A Two-Dimensional Analysis of the Flowfield and Performances of Linear Aerospikes During Differential Throttling

aerospace

MDPI

Article

A Two-Dimensional Analysis of the Flowfield and Performances of Linear Aerospikes During Differential Throttling

Jehangir Hassan, Gaetano Maria Di Cicca, Michele Ferlauto, Roberto Marsilio * and Emanuele Resta

Department of Mechanical and Aerospace Engineering, Politecnico di Torino, Corso Duca degli Abruzzi 24, 10129 Torino, Italy; jehangir.hassan@polito.it (J.H.); gaetano.dicicca@polito.it (G.M.D.C.); michele.ferlauto@polito.it (M.F.); emanuele.resta@polito.it (E.R.)

* Correspondence: roberto.marsilio@polito.it

Abstract: The performances of two linear aerospike nozzles, generated by truncating the same plug contour at 40% and 20% of its ideal length, are investigated numerically within a two-dimensional approximation and compared with each other. The nozzle geometry is a 2D representation, extracted from the CAD model of the actual nozzles under experimental investigation. In the working conditions studied here, the nozzle is throttled differentially, by setting different flow conditions on the upper and lower inlet, with the aim of generating thrust vectoring effects. The performances and flowfield of both aerospikes are investigated for values of the nozzle pressure ratio (NPR) ranging from 3.7 up to the design condition (NPR = 200), and for several levels of differential throttling. The CFD approach adopted is based on a two-dimensional RANS flow model. Comparisons between the numerical and experimental data are performed at two nozzle working conditions: without and with differential throttling. The numerical results are in good agreement with the experimental data. Moreover, the numerical simulations of the throttling case have shown a thrust deflection of about 5 degrees, with a differential pressure of approximately 10 percent.

Keywords: aerospike nozzle; fluidic thrust vectoring; supersonic nozzles; rocket nozzles

Academic Editor: Sergey Leonov

Received: 23 January 2025
Revised: 26 February 2025
Accepted: 27 February 2025
Published: 28 February 2025

Citation: Hassan, J.; Di Cicca, G.M.; Ferlauto, M.; Marsilio, R.; Resta, E. A Two-Dimensional Analysis of the Flowfield and Performances of Linear Aerospikes During Differential Throttling. *Aerospace* **2025**, *12*, 200. https://doi.org/10.3390/aerospace12030200

1. Introduction

In recent years, an increasing number of private aerospace companies have been involved in space exploration programs. The competition between them is encouraged by governments by awarding contracts for the same space mission to multiple contractors. Some examples of this new wave in aerospace activities are as follows: the Virgin Galactic Spaceplane and LauncherOne; the SpaceX highly successful Falcon-9 space launcher along with its crewed spacecraft Dragon capsule; Blue Origin's New Shepard and New Glenn rocket systems; the Electron space launcher of RocketLab; and the rocket systems of the United Launch Alliance (ULA). A key role in this competition is played by the reduction in the mission costs. One of the most successful design strategies in this direction has been the introduction of reusable launchers. In turn, launcher reusability justifies the introduction of more effective and complex propulsion systems, since the related costs will be spread over multiple missions.

Simultaneously, the research on achieving performance gains through reducing thrust-loss and perfect adaptation of the exhaust flow to changing environment pressure have focused on advanced nozzles [1]. Nowadays, thrust vectoring is becoming increasingly important to enabling the recovery of the first stages of launch vehicles (for example the Falcon-9 reusable/reflight rocket and the Super Heavy Booster of SpaceX), allowing for a

reduction in launch costs [2–4]. Such techniques do not need mechanical devices and may potentially integrate retro-propulsion features [5].

Until now, space launchers have utilized traditional bell-shaped nozzles designed to work in adapted conditions at a certain altitude. Before and after that altitude, thrust losses arise. Up to 15% thrust-loss was reported in the main engines of the NASA Space Shuttle during launch under high over-expanded nozzle conditions [1,6]. The pursuit of efficient nozzles with altitude self-adapting features led researchers to design multiple types of advanced nozzles, with particular interest on the dual-bell nozzle [1,7] and to the more promising plug nozzle [8–10] and aerospikes [11–13]. An aerospike nozzle was selected for the propulsion system of the reusable launch vehicle (RLV) X-33 program [1,14], which was a Single Stage to Orbit (SSTO) vehicle. During project CALVEIN (California Launch Vehicle Education Initiative), many tests were conducted to analyze the truncated plug nozzle [10]. Some other private companies involved in proposing designs for aerospike engines for space vehicles include Firefly Aerospace, RocketStar Space, and ARCA Space corporation [15]. In the case of a linear aerospike nozzle, it may have a single rectangular nozzle or clustered quasi-rectangular nozzle modules n on both sides. Such configurations make it a useful platform for implementing multiple strategies of thrust vector control (TVC). Thrust vector control helps align the vehicle thrust with the vehicle center of gravity to maintain its flight path or to steer it as desired. FTV has advantages in its simplicity, low-weight, and fast response time [3,16–19]. For the reader interested in fluidic thrust vectoring applied to several types of advanced nozzle, refer to Refs. [20,21] for a review.

The high performances that can be achieved by aerospike nozzles drive ongoing theoretical, numerical, and experimental efforts to understand their self-adaptive capabilities and enhance their aero-thermal characteristics [12,14,22]. Alongside the research on nozzle cooling for space launcher applications, studies have also been conducted on aerospike flow control to vectorize thrust [15,23,24]. Concerning this topic, numerical studies on the control and vectorization of thrust have been underway at the Politecnico di Torino for a decade, considering different types of advanced nozzles and thrust vectoring technologies [25,26]. Recently, one study focused on the linear aerospike nozzle. The baseline of a linear plug nozzle was designed and two different aerospike nozzles were derived by truncating the plug at 20% and 40% of its ideal length. The flow features of such nozzles have then been investigated by numerical studies and experimental testing. Flowfield characterization was conducted by three-dimensional CFD simulations for the unthrottled case of the aerospike with 40% plug truncation. The entire flow inside and outside the aerospike nozzle was simulated [27]. The numerical results were compared with the experimental data successfully and were used to characterize the flow internal structure, which is very complex, especially at low NPR. The CFD simulations were also used to complete the analysis on the range of operating conditions at NPR not reached by experimental testing.

The aerospike nozzle models studied here have individual chambers for the upper and lower outlets, which can be throttled differentially in order to achieve asymmetric expansions and thus lateral force components. Thrust vectoring is, therefore, obtained by differential throttling.

In this paper, we conduct a two-dimensional numerical analysis of cold flow under various expansion ratios and throttling conditions for aerospike nozzles. The effects of the hot gas flow and the interaction between the nozzle and the combustion chamber have been analyzed in [28,29]. This approach is feasible because, during the design process of the aerospike nozzle models, we carefully selected geometric parameters and ratios to achieve an almost two-dimensional flow over the nozzle plug. Moreover, the 2D approach is valuable for developing dynamic models for nozzle control applications. Lower-order modeling of the system unsteady response is typically necessary for control

design. The nozzle response during thrust vectoring can be determined through a series of flowfield unsteady simulations. A full-range analysis of the nozzle dynamic response using 3D simulations would be prohibitively expensive. This study is expected to contribute to the static and dynamic characterization of fluidic thrust vectoring in advanced nozzles, providing valuable support for the development of SSTO launch vehicles. The paper is structured as following: first, we describe the nozzle setup, geometry, and throttling technique; this is followed by the mathematical model, numerical method, and boundary conditions. Next, we introduce a throttling parameter, *DF*, which quantifies the pressure mismatch between the upper and lower inlets. Finally, we analyze the performance of the two designed nozzles across a wide range of NPR and throttling conditions.

2. Nozzle Model Description

The two nozzle models presented here are both derived from the same plug profile, designed using the classical approach proposed by Angelino [30]. The main design parameters include a pressure ratio $\mathrm{NPR}_d = 200$, a tilt angle ϑ at the throat of 68.1 degrees, and a width-to-height throat ratio $b/h_t = 30.41$. A summary of other relevant parameters is provided in Table 1.

Table 1. Dimensions and main parameters of the designed nozzle models.

Quantity	Symbol	Value
Ideal plug length	L_{max}	133.53 mm
Length of 40% plug	L_{40}	53.41 mm
Length of 20% plug	L_{20}	26.70 mm
Base height (LASN-40)	h_{b40}	12.22 mm
Base height (LASN-20)	h_{b20}	25.63 mm
Width of single throat	b	77.55 mm
Height of single throat (sub-nozzle)	h_t	2.55 mm
Width-to-height throat ratio	b/h_t	30.41
Area of both throats	A_t	395.51 mm^2
Height of nozzle exit	h_e	64.52 mm
Aerospike nozzle exit area	A_e	5003.21 mm^2
Aerospike nozzle area ratio	A_e/A_t	12.65

On the basis of previous work [24], the aerospike nozzle models have been generated by truncating the plug profile at 40% (LASN-40) and 20% (LASN-20) of its ideal length, respectively. The simplified CAD models and a sketch of the nozzle sections at the symmetry plane are shown in Figure 1. The nozzle geometries of this analysis were extracted from the corresponding CAD model. Further information about the nozzle design and experimental setup can be found in [31,32].

As illustrated in Figure 1, the nozzle internal geometry features two distinct chambers that supply the upper and lower sub-nozzle outlets. As sub-nozzles, the intention is for the internal channels to direct the airflow from the stagnation chambers to the plug profile. In Figure 1a, the sub-nozzles of LASN-40 are highlighted with two small dashed circles. Since, in present geometries, the outlets are the sections of minimum area, they are also defined as 'throats'.

By supplying the two chambers with distinct pressure levels, i.e. by differential throttling, two distinct expansions are generated on the upper and lower profile of the nozzle plug. This results in a transverse component of the force acting on the nozzle itself, thereby influencing the thrust.

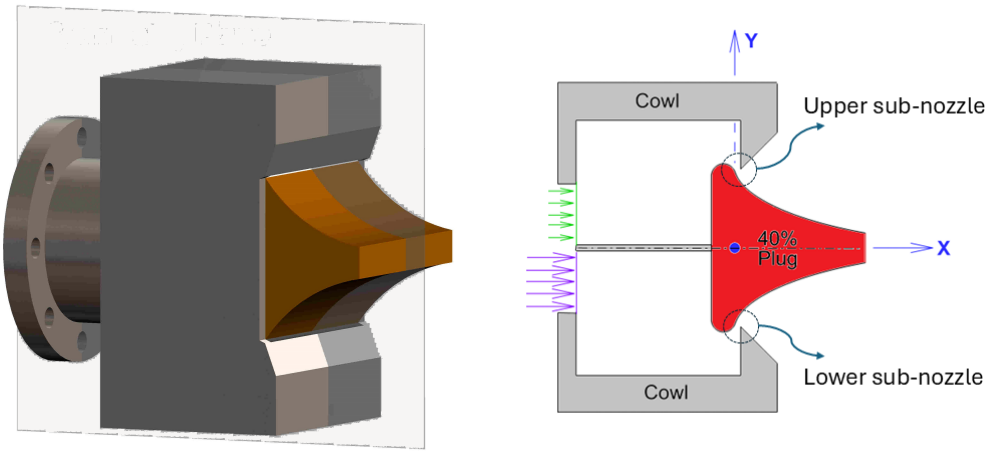

(**a**)

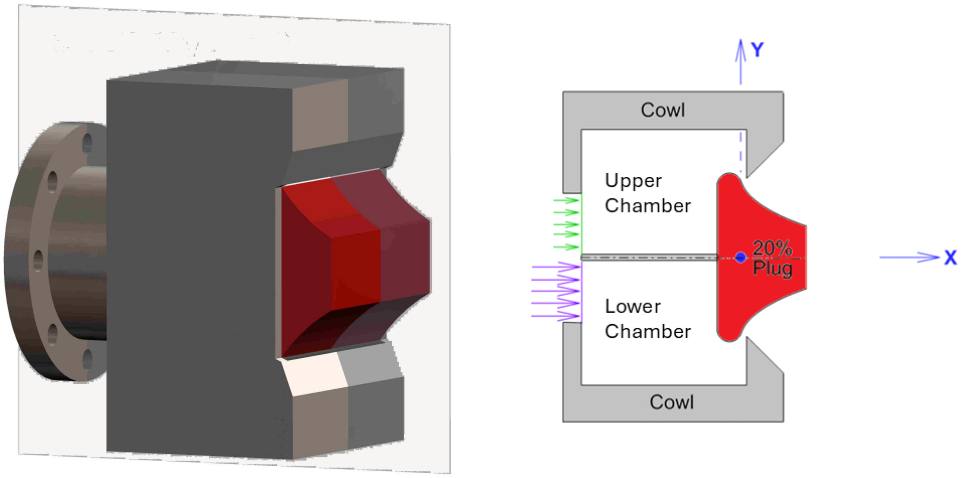

(**b**)

Figure 1. Sketch of the CAD model and symmetry section of the linear aerospike nozzles. (**a**) Aerospike nozzle LASN-40. (**b**) Aerospike nozzle LASN-20.

3. Mathematical Model and Numerical Method

The numerical framework adopted in this study will be briefly illustrated in this section. The flow inside and outside the nozzle is described by the compressible Reynolds Averaged Navier–Stokes (RANS) equations. The numerical computations have been carried out using the computational fluid dynamics (CFD) software ANSYS-Fluent [33]. Conservation equations for mass, momentum, and energy are solved within a finite volume approach in the compressible case. The Advection Upstream Splitting Method (AUSM), as a flux–vector splitting scheme, is used in the implicit scheme of integration.

The perfect gas equation was chosen as the model for the equation of the state of the working fluid, which is dry air. Its thermo-physical characteristics are determined as a function of temperature by means of Sutherland's Law for the dynamic viscosity μ and the thermal conductivity κ. The closure of the system of equations is achieved with the Spalart–Allmaras (S-A) one-equation turbulence model [34]. The S-A model is one of the four turbulence models recommended for nozzle flow simulations in Ref. [35], among fourteen different models investigated. Extensive testing and validation of the proposed numerical solver can be found in the literature [35] and have also been conducted by our group [25,31,32].

As mentioned, the nozzle geometries have been extracted from the manufacturing CAD models. The computational domains along with their meshes for LASN-40 and LASN-20 are shown in Figure 2, where the labels identify different parts. Green- and cyan-colored lines represent the upper and lower inlets (one for each section of the chamber), respectively, while blue lines represent the outlet boundary and farfield of the domain. All other surfaces are the walls of the models. The centerline is marked to identify the longitudinal symmetry of the models.

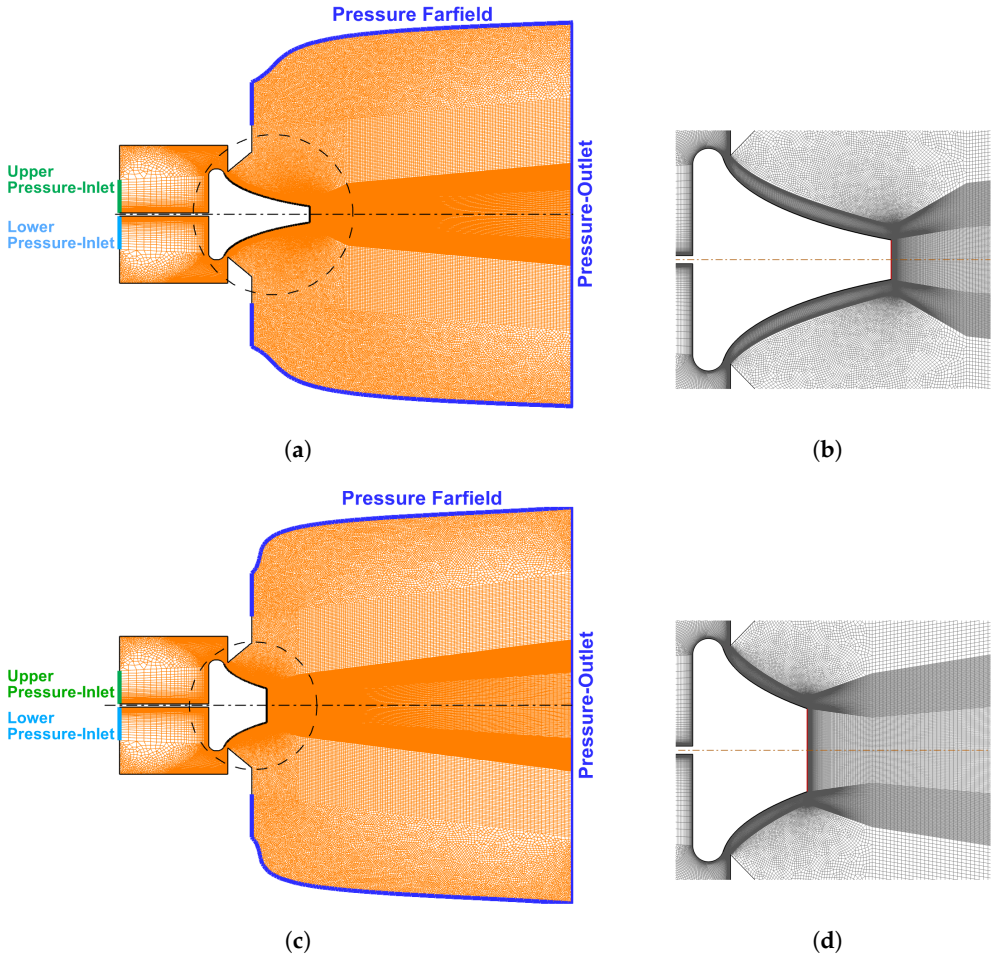

Figure 2. Sketch of the computational meshes and boundary conditions for the LASN-40 (**a**) and LASN-20 (**c**) geometries. (**b**,**d**) Zoom of the two grids in the region around the aerospike plug.

As visible in Figure 2, the grids are hybrid, with transfinite meshes surrounding the plug and other regions of interest, thereby creating a higher grid density to resolve the boundary layer. The Reynolds number, based on the nozzle exit height, ranges from an order of 10^6 to 10^9.

The boundary conditions are also shown in Figure 2a,c for both nozzles. Inlets are considered as pressure inlets, while outlets are defined as pressure outlets and pressure farfield. All the walls have been treated as no-slip adiabatic stationary wall boundaries. The farfield boundaries of the domain are generally set to freestream conditions, where the values of static pressure, static temperature, and freestream Mach number are imposed. For an efflux in calm air one may either set a very low Mach number value or set the far-field boundaries as pressure outlets. In this paper, the nozzle flow is supposed to exit into ambient with calm air. On the outlet boundaries, we, therefore, imposed ambient pressure, P_a. The ambient pressure has also been assumed as reference pressure. In all the simulations proposed, the ambient pressure was set to P_a = 101,325 Pa, while the ambient

air temperature was $T_a = 300$ K. The conditions imposed at the domain boundaries follow the guidelines of Poinsot and Lele [36] for supersonic and subsonic mixed flows. Finally, the upper and lower inlets, which have been defined as pressure inlets, were imposed with prescribed total temperature, pressure, and flow direction. In the present study, the outlet pressure was maintained at the constant value of ambient pressure, while the pressure at the nozzle inlets was set according to the desired level of nozzle pressure ratio NPR. The simulated NPRs were 3.7 to 200.

For the simulation without differential throttling (i.e., for the unthrottled case), both inlets were set at the same pressure level according to a prescribed NPR. For the simulations with differential throttling, the lower-inlet remained fully open, whereas the upper-inlet was throttled. A new parameter, the differential factor (DF), defined as

$$DF = 100\,\frac{(P_B^o - P_T^o)}{P_B^o} = 100\left(1 - \frac{\mathrm{NPR}_T}{\mathrm{NPR}_B}\right) \tag{1}$$

was introduced in order to describe the differential throttling conditions in a non-dimensional way. The variables P_T^o and P_B^o are the total pressure at the top and bottom chamber, respectively, whereas $\mathrm{NPR}_T = P_T^o/P_a$ and $\mathrm{NPR}_B = P_B^o/P_a$. The parameter DF, therefore, represents the percent of pressure mismatch in the upper chamber with respect to the bottom chamber, that is, $DF = 0$ shows the unthrottled case, whereas $DF = 100(1 - 1/\mathrm{NPR}_B)$ means upper inlet fully closed. In fact, the lowest value of the pressure at the throttled upper inlet P_T was equal to P_a when inlet was fully closed. As mentioned, in the present analysis, the lower inlet always remained fully open.

The criteria adopted for meshing were chosen to accurately capture the pressure distribution over the plug surface of the aerospike nozzles. A grid convergence analysis was conducted. Simulations at NPR = 3.7 for the unthrottled case were performed on a coarse grid (109 *k*-cells), a medium grid (162 *k*-cells), and a fine grid (265 *k*-cells). The results were then compared in terms of the pressure distribution on the plug surface, as shown in Figure 3. Given the good results obtained with the medium grid, it was decided to use this grid for all remaining simulations.

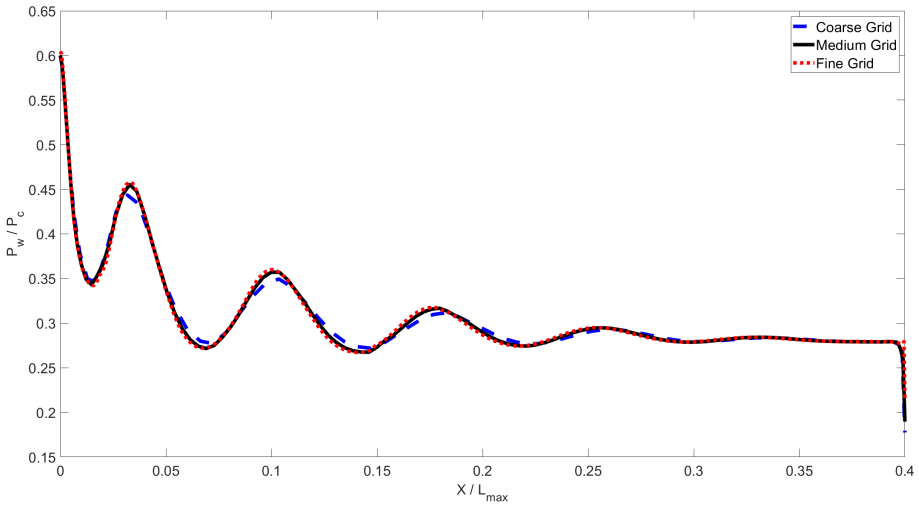

Figure 3. Grid convergence. Comparison of the pressure distributions over LASN-40 plug profile at NPR = 3.7 and DF = 0, computed on a coarse (109 *k*-cells), a medium (162 *k*-cells), and a fine grid (265 *k*-cells).

4. Numerical Results

In this section, the results of the two-dimensional CFD study of the aerospikes flowfield and performances are presented. The analysis is organized as follows: First, we provide a validation of the 2D numerical framework against the experimental results. Then, the nozzle performances and flowfield are studied at different NPRs for the unthrottled case (DF = 0) and also for the working DF-values at selected NPRs. The flowfield characteristics of the two aerospikes and the other performance aspects are finally discussed.

4.1. Validation of the Numerical Method

The effectiveness of the numerical setup is validated here by several test cases. An in-house experimental setup was used for testing and to characterize the propulsive nozzles, with a special focus on advanced and vectored nozzle concepts. The experimental setup is described in Refs. [31,32] in detail.

The validation of the numerical framework was performed for both aerospikes under conditions of NPR = 3.7, without and with the use of differential throttling. With a design pressure ratio of $\mathrm{NPR}_d = 200$, the nozzles were worked in this case in an extremely over-expanded condition. This working condition was the most suitable for validation with experimental data since it is characterized by a high sensitivity of the flowfield to variations in chamber pressure, and thus to the NPR. The situation is clearly visible, for instance, in Figure 4b, where the contour of absolute pressure field is presented. After an initial expansion close to the outlet, the flow interacts with an external pressure field, characterized by higher values than those expected at design conditions, and a series of recompression and expansion waves are formed along the aerospike profile. The phenomenon is non-linear and the number and loci of these local maxima and minima of the pressure field are highly dependent on the expansion ratio. A relatively small variation in NPR leads, in fact, to changes in the structure of the supersonic jet, shifting the reflection points of the compression and expansion waves along the wall, thereby altering the entire pressure distribution along the surface of the nozzle wall.

The comparison between experimental and numerical data for the LASN-40 is presented in Figure 4. Both the symmetric case, without differential throttling ($DF = 0$), and the case with $DF = 6.22\%$ are shown. In the former case, the pressure distributions along the plug top and bottom walls are symmetric and in good agreement with the experimental data (Figure 4a).

In the case with differential throttling, the pressure distributions on the top and bottom surfaces of the spike differ from each other. Both distributions closely match the experimental measurements, as displayed in Figure 4c. Figure 4c,d highlights the system sensitivity to chamber pressure mismatch. A 6% difference between the chamber pressures leads to an appreciable deviation in the positions of local maxima and minima on the plug surfaces.

An analogous comparison is proposed for the LASN-20 aerospike in Figure 5. As the plug length is half of that of LASN-40, we note that in this case the wall collects a lower number of compression and expansion waves. In particular, from Figure 5a,b for the symmetric case, we note the presence of three of the five maxima observable in the previous case. It can also be noted that the numerical pressure curves in both truncation cases overlap well, highlighting that in the case of two-dimensional simulations, wall truncation weakly affects the pressure distribution, and the expansion occurs in the same way almost up to the truncation, independently of the chosen truncation length. This is largely due to the fact that the region involved is supersonic and therefore less influenced by external conditions.

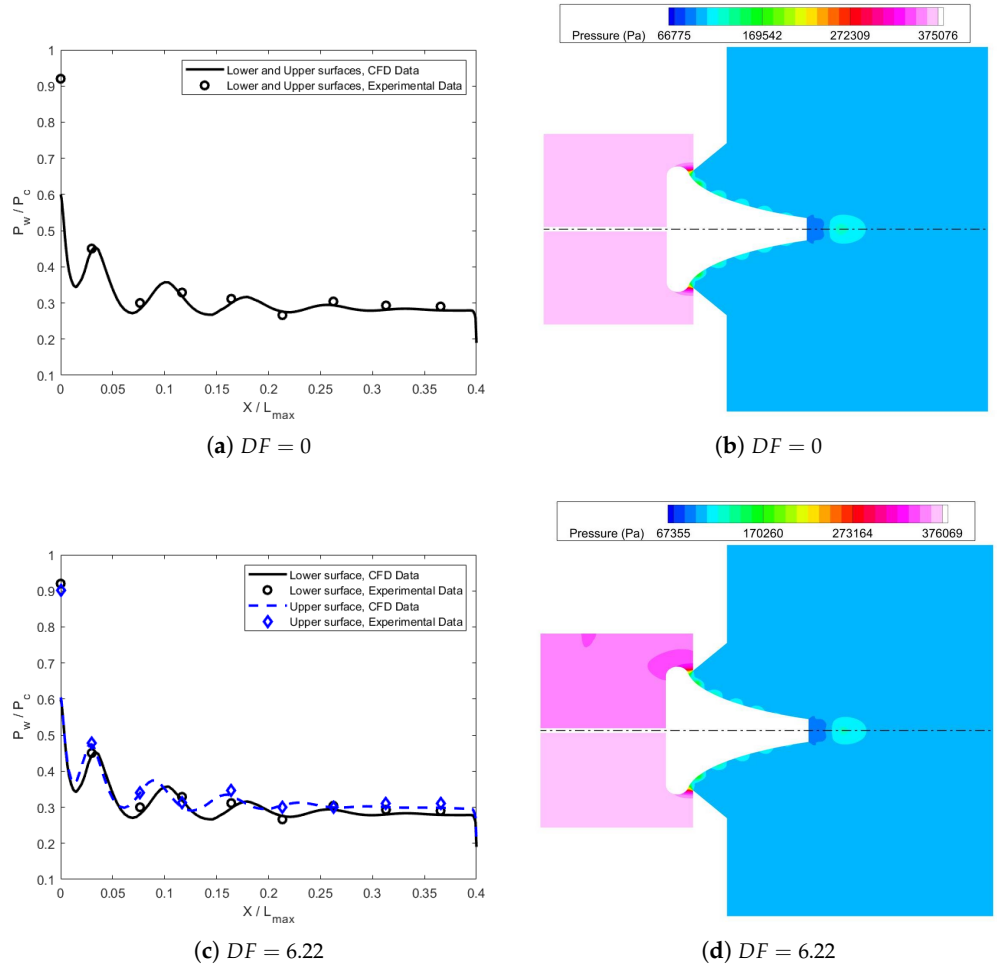

(**a**) $DF = 0$ (**b**) $DF = 0$

(**c**) $DF = 6.22$ (**d**) $DF = 6.22$

Figure 4. Validation case. Comparison of the numerical and experimental pressure distributions over the LASN-40 plug at NPR $= 3.7$ for (**a**) $DF = 0$, (**c**) $DF = 6.22$, and (**b**,**d**) corresponding pressure fields.

A similar situation is observed for the numerical test with differential throttling. The experimental data are also in good agreement with the wave system related to this configuration (Figure 5c). It should be pointed out that when comparing the pressure distributions on the LASN-40 and LASN-20 plug walls for the two throttled cases, they do not match perfectly because for the LASN-20 the differential factor has been set to a slightly lower value ($DF = 6.2\%$), corresponding to that measured in the experimental tests we performed.

Comparisons at remarkably different pressure ratios currently have not achieved for the actual experimental setup. The same numerical framework has otherwise been validated with a similar aerospike model, for which the experimental data are available in the literature over the full range of working conditions [24]. It was observed that as the nozzle pressure ratio becomes higher and higher, the wave system tends to disappear and the pressure matching between numerical and experimental data becomes even closer.

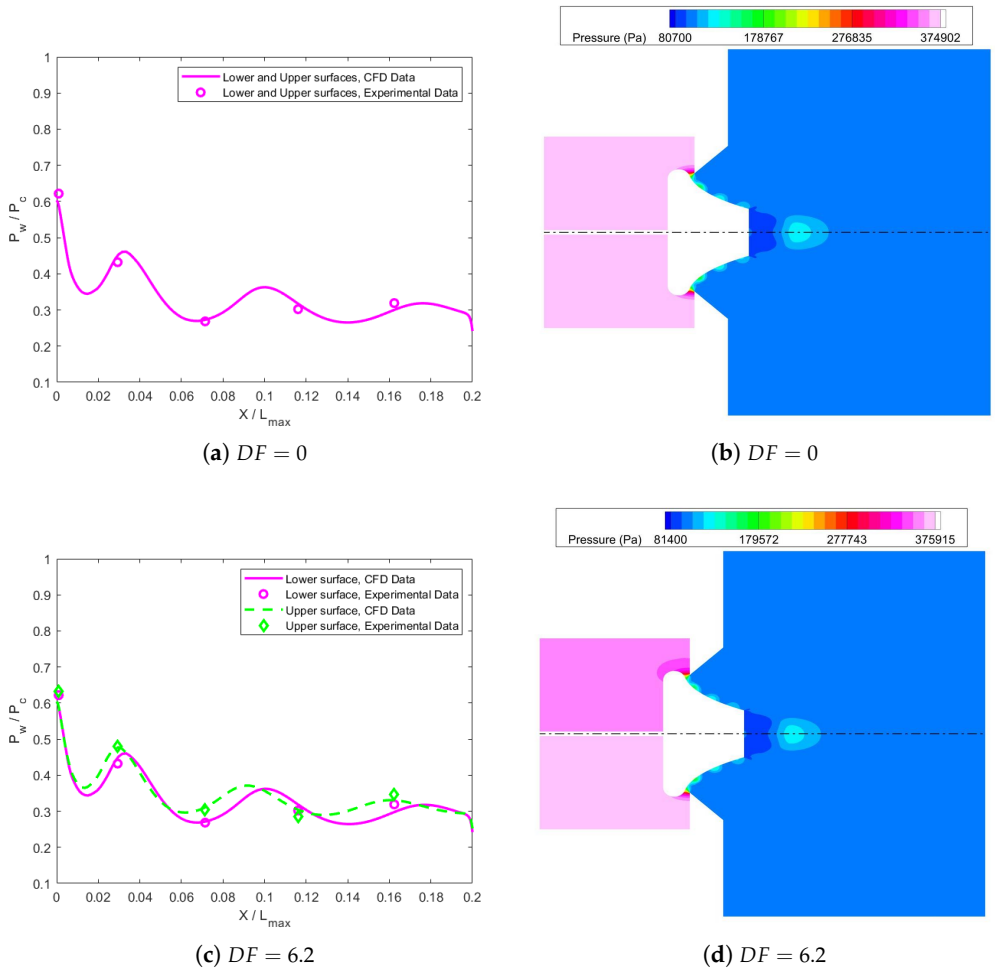

(**a**) $DF = 0$ (**b**) $DF = 0$

(**c**) $DF = 6.2$ (**d**) $DF = 6.2$

Figure 5. Validation case. Comparison of the numerical and experimental pressure distributions over LASN-20 plug at NPR $= 3.72$ for (**a**) $DF = 0$, (**c**) $DF = 6.2$, and (**b**,**d**) corresponding pressure fields.

4.2. Flowfield and Performances in the Unthrottled Case

This section is devoted to the study and comparison of the flow features of both aerospike nozzles, their performance, and their ability to self-adapt to the altitude, that is, how the performances varies with the expansion ratio. This analysis is essential for understanding the flow structure at various NPRs. It is well known from the literature [1] that aerospikes may exhibit two main flow configurations (closed wake and open wake) with the variation in NPR.

This study was conducted over the range $3 <$ NPR $<$ NPR$_d$. For conciseness, only some representative nozzle flowfields and operating conditions are proposed and discussed in next sections. This study over the operating range without differential throttling provides information on what happens to the flowfield around the aerospike under symmetric forcing, and it may also reveal possible strategies to make the flow asymmetric at lower energy costs at the various working conditions.

4.2.1. Flowfield Analysis

We start by analyzing three typical operating conditions, that is, low, medium, and high values of NPR. The results for the two aerospikes (LASN-40 and LASN-20) are discussed simultaneously and shown side-by-side in order to highlight the flow similarities and differences obtained as an effect of the different truncations of the same plug profile.

Let us consider the case with a nozzle expansion ratio NPR = 4.2. Although it is slightly higher than that characterizing the test case in the previous section, this variation is sufficient to alter the flow pattern.

The number of pressure peaks generated by the recompression and expansion waves reduced to four for the LASN-40 and to two for the LASN-20, corresponding to the low-mach zones in Figure 6a,b. These figures display the flowfield inside and outside the aerospikes through the Mach contour maps. A more immediate comparison may be made by counting the local pressure peaks at the various NPR values, as shown in Figure 7a, which shows the normalized pressure distribution P_w / P_c on the plug wall for both aerospikes.

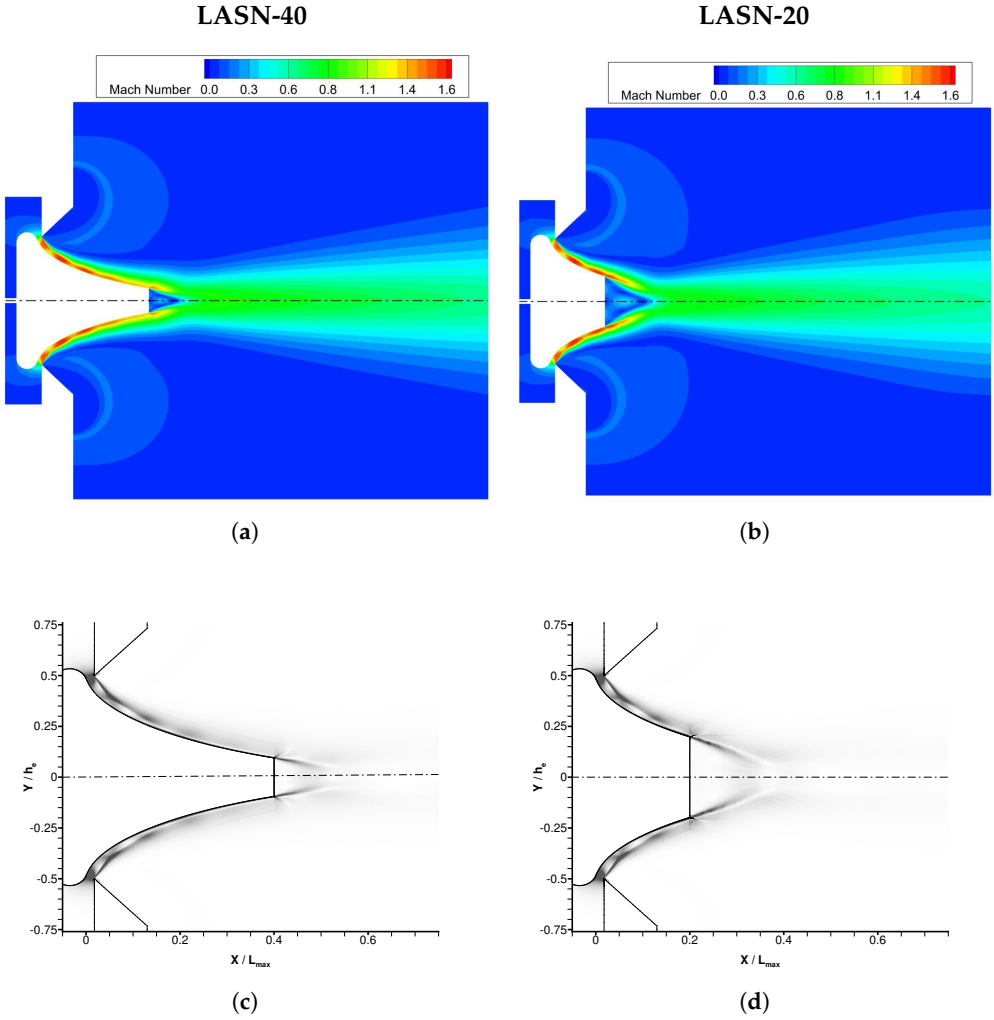

Figure 6. Unthrottled test case. Mach number contours (**a**,**b**) and numerical Schlemiel (**c**,**d**) for LASN-40 and LASN-20 at NPR = 4.2.

The Mach number representation of the flowfield (Figure 6a,b) highlights regions of high and low speed, particularly distinguishing between subsonic and supersonic zones. This flow pattern representation is accompanied by numerical Schlemiel images shown in Figure 6c,d for the LASN-40 and LASN-20, respectively. Schlieren images are typically used in experimental investigations, but in CFD practice, they are usually proposed for comparing numerical solutions with actual experimental Schlieren images. The numerical Schlieren images are derived from the absolute value of the density gradient, which is a composite function of temperature and pressure. These images highlight regions where large variations occur as a result of temperature or pressure gradients. In this context, they serve as complementary information, emphasizing the regions with large gradients in the

thermodynamic properties of the fluid. In Figure 6c,d, the light regions represent areas with minimal variation in density, whereas the dark regions represent areas with significant variation. Ignoring the larger wake on the truncation of LASN-20 compared to LASN-40, differences between the two gradient patterns generated on the plug profile are very small in the range $X/L_{max} < 0.2$, with a substantially identical pattern between Figure 6c,d.

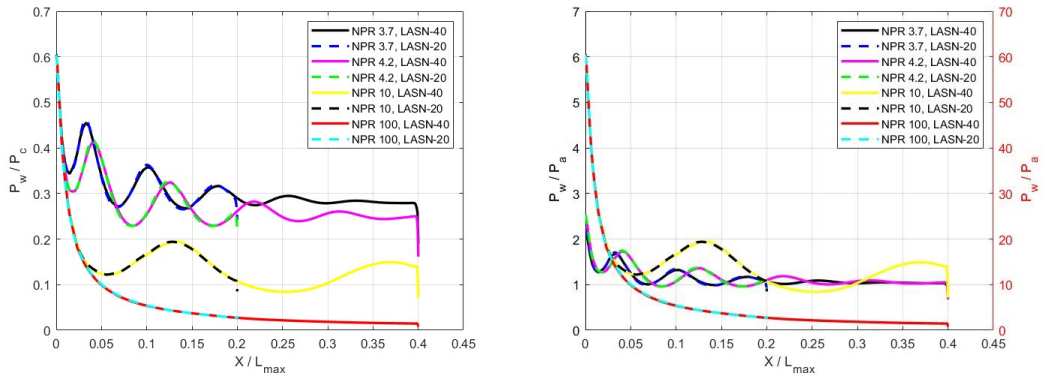

(**a**) (**b**)

Figure 7. Unthrottled test case. Pressure distributions P_w/P_c (**a**) and P_w/P_a (**b**) along the LASN-40 and LASN-20 plug profiles at NPR $= 3.7, 4.2, 10$ and 100.

The subsequent analysis of the flow field was conducted at NPR $= 10$. Although the degree of overexpansion was still very high since the NPR was only one twentieth of the design one, the recompression and expansion regions reduced in number and expanded in the extension (see Figure 8a,b). We essentially notice two large low-pressure zones along the LASN-40 plug in Figure 8c, corresponding to the two pressure minima visible in Figure 7a. For the LASN-20, the second cell already falls half into the region of influence of the truncation and therefore shows a more complex interaction.

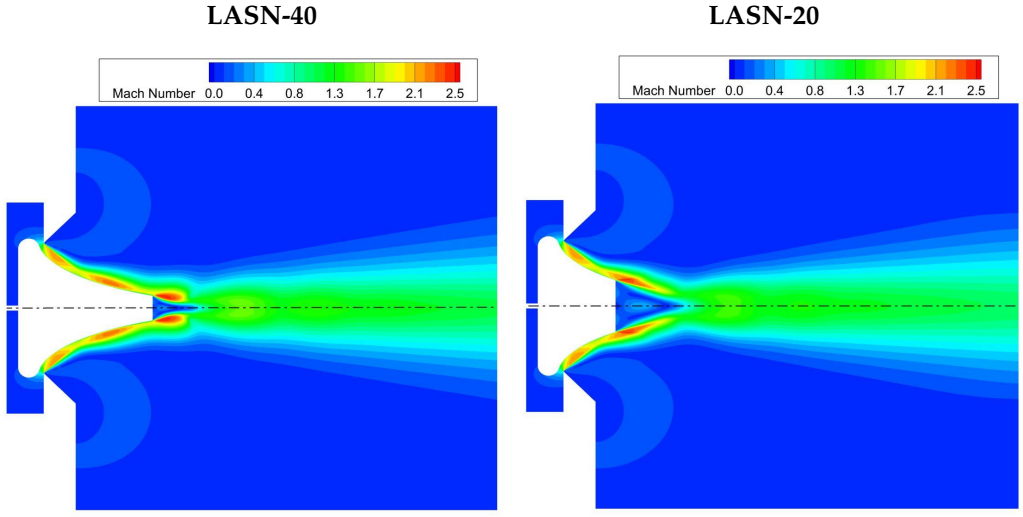

(**a**) (**b**)

Figure 8. *Cont.*

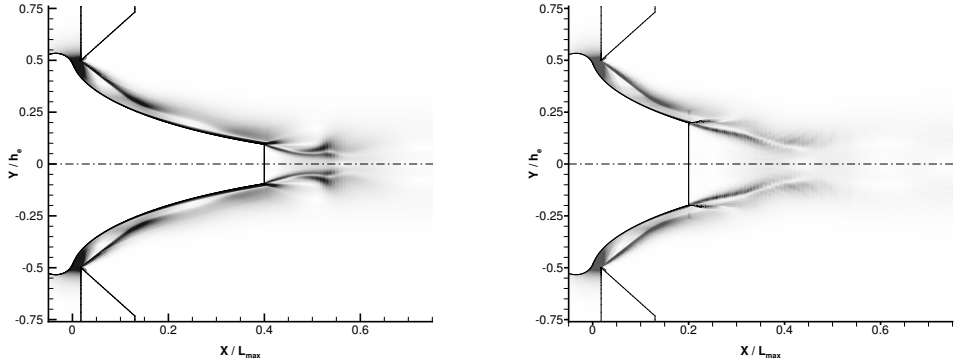

(**c**) (**d**)

Figure 8. Unthrottled test case. Mach number contours (**a**,**b**) and numerical Schlieren (**c**,**d**) for LASN-40 and LASN-20 at NPR = 10.

At NPR = 100 = 0.5NPR$_d$, the flow structure of the plug becomes the definitive one, without wave phenomena, and is morphologically completely comparable to the design one. The differences between the flow fields depend on the different domains of influence due to the different truncations and the shapes of the relative wake (see Figure 9).

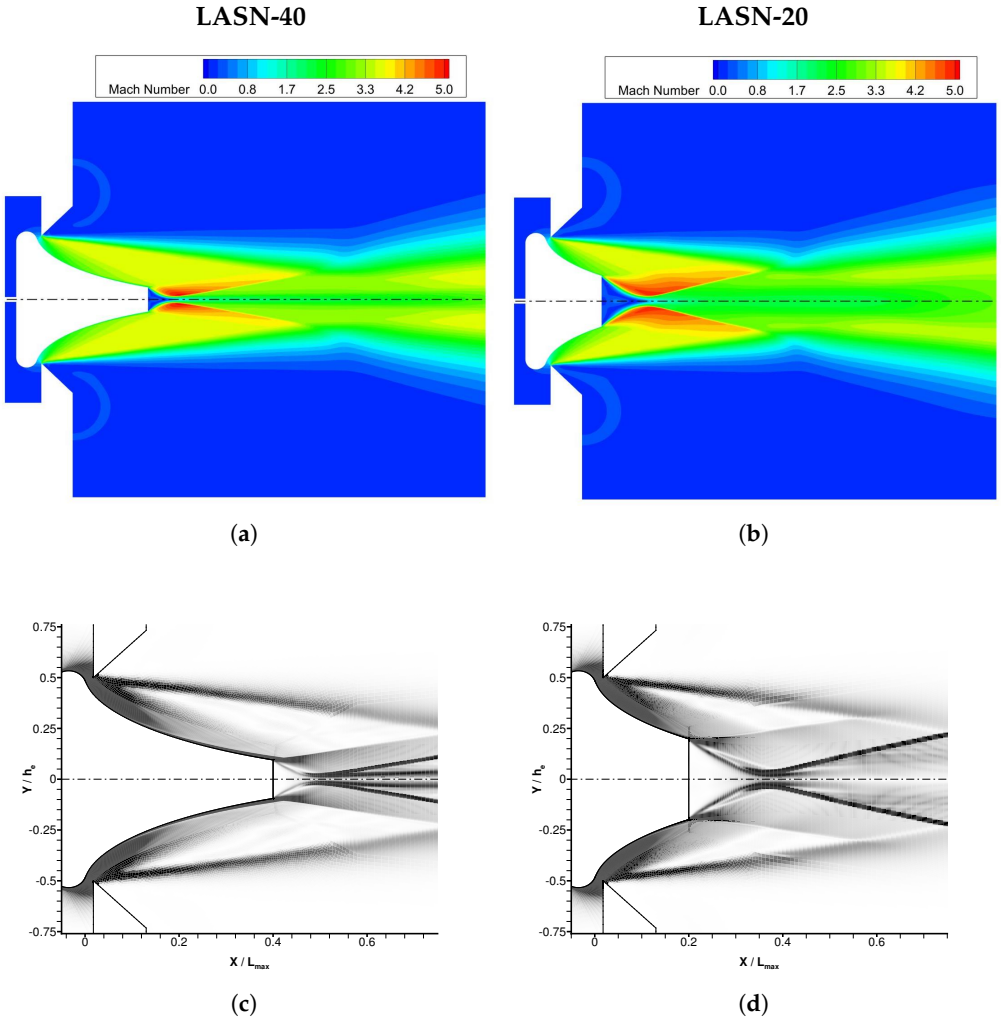

(**a**) (**b**)

(**c**) (**d**)

Figure 9. Unthrottled case. Mach number contours (**a**,**b**) and numerical Schlieren (**c**,**d**) for LASN-40 and LASN-20 at NPR = 100.

More generally, it is observed that both nozzles realize the same flow in the outlet region. The situation obtained in this region is highlighted in Figure 10 for NPR = 4.2, 10, 100, and 200.

The Mach contour lines of both nozzles are perfectly superposed. The same observation can be made looking at Figure 7, where the wall pressure P_w is shown as both normalized with the chamber pressure P_c and with the ambient pressure P_a. In both diagrams, it is noted that the curves relative to the two nozzles are perfectly superimposed within the range $0 < x/L_{max} < 0.2$.

Therefore, we can conclude that the difference in performance and flow structure between LASN-40 and LASN-20 is primarily influenced by the truncation length, which effects the size of the wake and the base pressure. However, the truncation only impacts the wedge region of the fluid dynamic field along the sides of the plug within the range of the NPR considered, up to the design conditions.

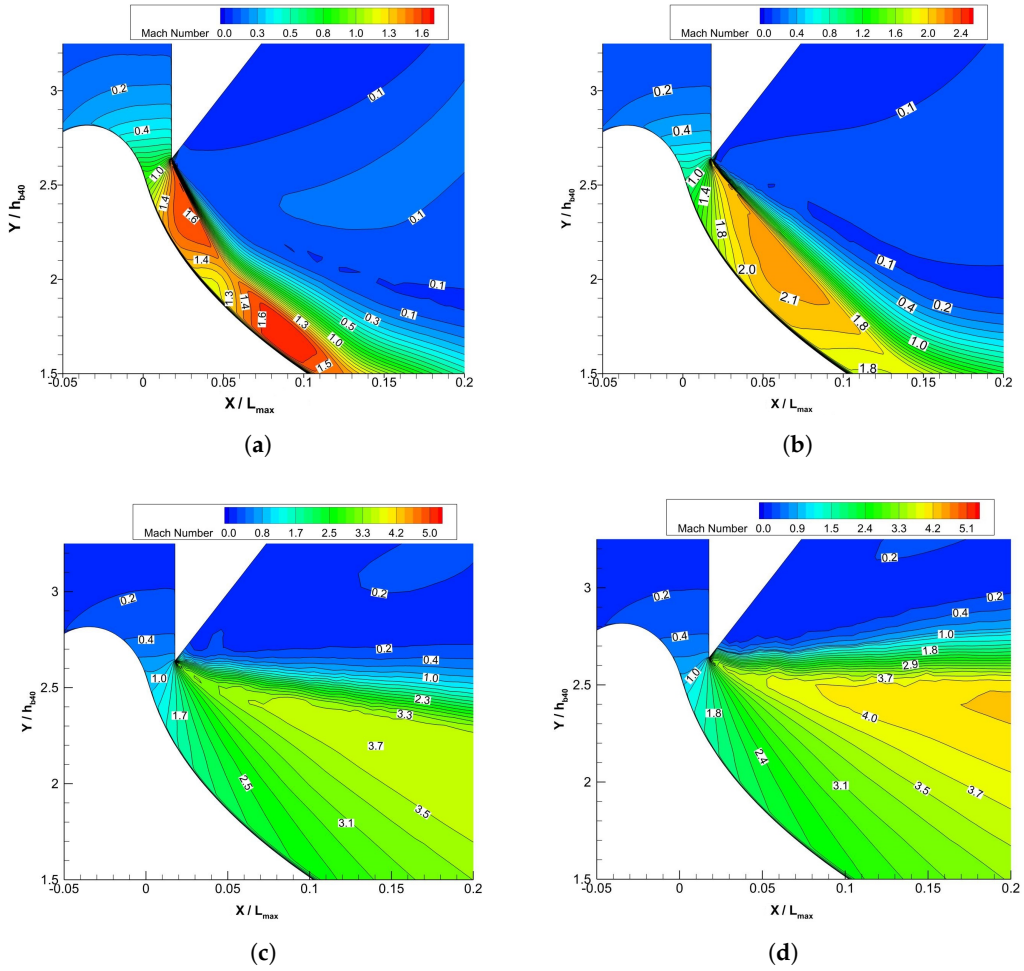

Figure 10. Mach number contours near throat of sub-nozzle of LASN-40 & LASN-20. (**a**) NPR = 4.2. (**b**) NPR = 10. (**c**) NPR = 100. (**d**) NPR = 200.

4.2.2. Nozzle Performances

Regarding the thrust trend, a study was conducted according to the same guidelines followed in [24]. For a rocket, or also for the gross thrust of an air-breathing engine, we may write:

$$\vec{T} = T_x\vec{i} + T_y\vec{j} = (\dot{m}_t\vec{V}_t)_B + (\dot{m}_t\vec{V}_t)_T + \int_{\mathcal{L}}(P - P_a)\vec{n}d\ell \quad (2)$$

where $\dot{m}$ is the mass flow rate and $\vec{V}$ is the flow velocity. The compound surface $\mathcal{L}$, as in Figure 11, is the sum of the plug surface from throat with the truncation included, and of the sub-nozzle throat surfaces. Therefore, both the jet flows exiting from the upper and lower sub-nozzle throats and the pressure distribution along the surface $\mathcal{L}$ contribute to the thrust vector. A sketch of the mentioned control surface $\mathcal{L}$ is shown in Figure 11. Only the upper side of the nozzle domain is shown in the figure. The same scheme applies to the bottom side and to the bottom sub-nozzle throat. Regarding the thrust trend in differential throttling, this study was conducted according to the same guidelines followed in [24].

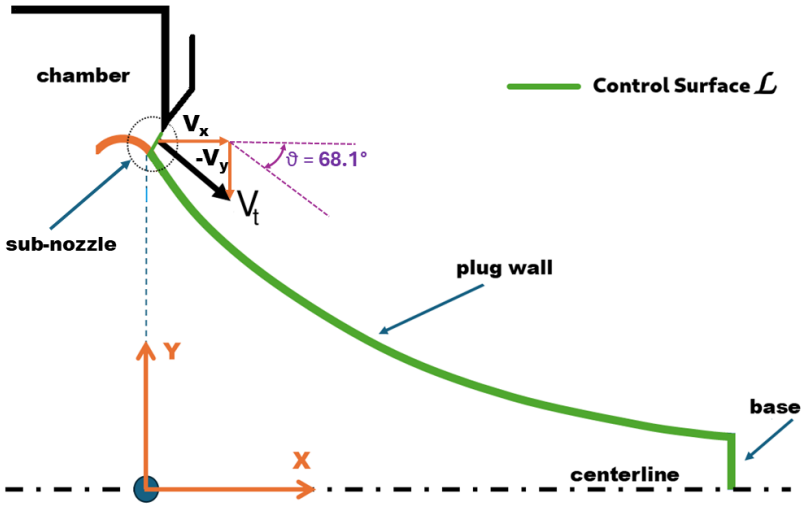

Figure 11. Definition of the control surface for nozzle thrust computation. Only the upper side of the nozzle domain is shown.

Ansys Fluent provides multiple tools to obtain momentum terms and pressure terms for the thrust in specified direction. Its built-in functions have been used to quantify the thrust contributions from the sub-nozzle in inclined position, plug wall and its local inclinations, and plug base.

In the symmetric case, we obtain that $T_y = 0$ and $\vec{T} = T_x\vec{i}$. The plot of the axial component of thrust T_x as a function of the nozzle pressure ratio has been evaluated from the CFD simulations according to Equation (2), and it is reported in Figure 12. The thrust values have been normalized by the design value T_{xo}. The analysis was performed by keeping the ambient pressure P_a constant; therefore, $P_c = \mathrm{NPR} \cdot P_a$. Under this hypothesis, it was then demonstrated that in Equation (2), the terms $\dot{m}_t\vec{V}_t$ were a linear function of NPR while it affected the pressure term in an inversely proportional manner. The overall trend is therefore the approximately linear one shown in the figure. This trend should not be confused with the one obtained in the study of the thrust of an aerospike engine with altitude. In that case, the pressure and temperature conditions in the chamber were kept constant, unlike the static pressure of the external environment as performed here to recreate the same conditions as the experimental tests.

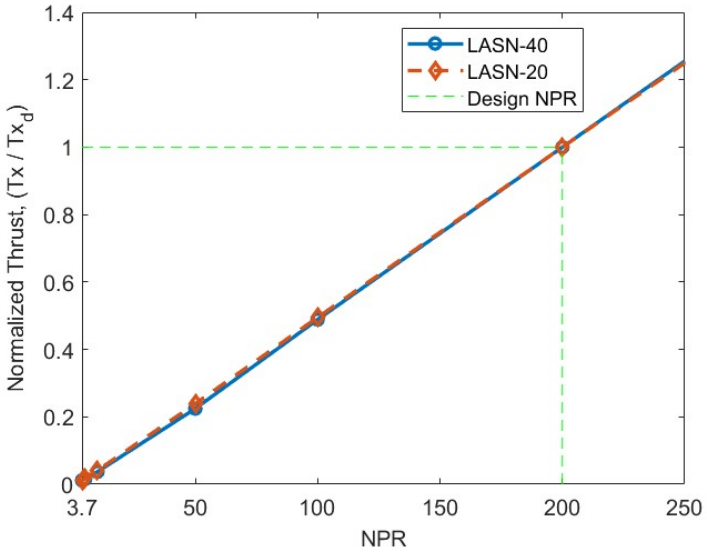

Figure 12. Unthrottled test case. Thrust as a function of the nozzle pressure ratio.

4.3. Flowfield and Performances with Differential Throttling

In this section, we proceed with the analysis by studying numerically, within the 2D model, the performances and the flowfield on the two aerospike nozzles when differential throttling is applied in order to vectorize the thrust.

The nozzle pressure ratio is also taken into account in the analysis, so that we consider a combined variation of NPR anf DF. The values $\text{NPR} = 5, 50, 200$ were chosen. These values differ from those in the study performed in the previous section to enrich the range of operating points presented. Therefore, the case with $DF = 0$, which corresponds to the unthrottled case, is always reported. Although different, these points fall anyway into scenarios similar to those proposed in the previous section. Moreover, the performance evaluations are based on a larger number of computed operating points than that proposed here. In fact, only the cases we considered the most significant, are proposed here.

4.3.1. Flow Features

As mentioned, the nozzle flow was studied at the values $\text{NPR} = 5, 50, 200$. At each NPR, the effect of applying different levels of differential throttling was then computed. As for the unthrottled case, the analysis was conducted simultaneously for both nozzles, proposing the results side by side, in order to highlight similarities and differences between the two aerospikes related to the effect of the different truncation.

After the cases $\text{NPR} = 3.7$ and $\text{NPR} = 4.2$, the condition with $\text{NPR} = 5$ was chosen to describe the behavior of the aerospikes at severely overexpanded conditions. The flowfields over the two nozzles are presented in Figure 13. The Mach contour maps are shown for the two aerospikes at several differential throttling conditions ($DF = 0, 10\%, 25\%, 50\%$). The unthrottled case ($DF = 0$) is shown first. As the essential feature of this type of nozzle, by means of the wake past the truncation, the flow aerodynamically generates the missing part of the spike (hence the name "aero" spikes), which somehow mimics the blockage effects but cannot behave as a solid surface, since it cannot sustain any force. The characteristic length of the wake depends on the width of the truncated base, since the truncation wedges impose the flow separations. The wakes are also strongly influenced by the conditions of the flow (speed, direction, pressure, etc.) reaching the wedges. These conditions then affect the subsequent interactions between recompression and expansion waves on the fluid surfaces, delimiting the recirculation zone of the aerospike base. These effects are seen to amplify with the increase in both NPR and DF.

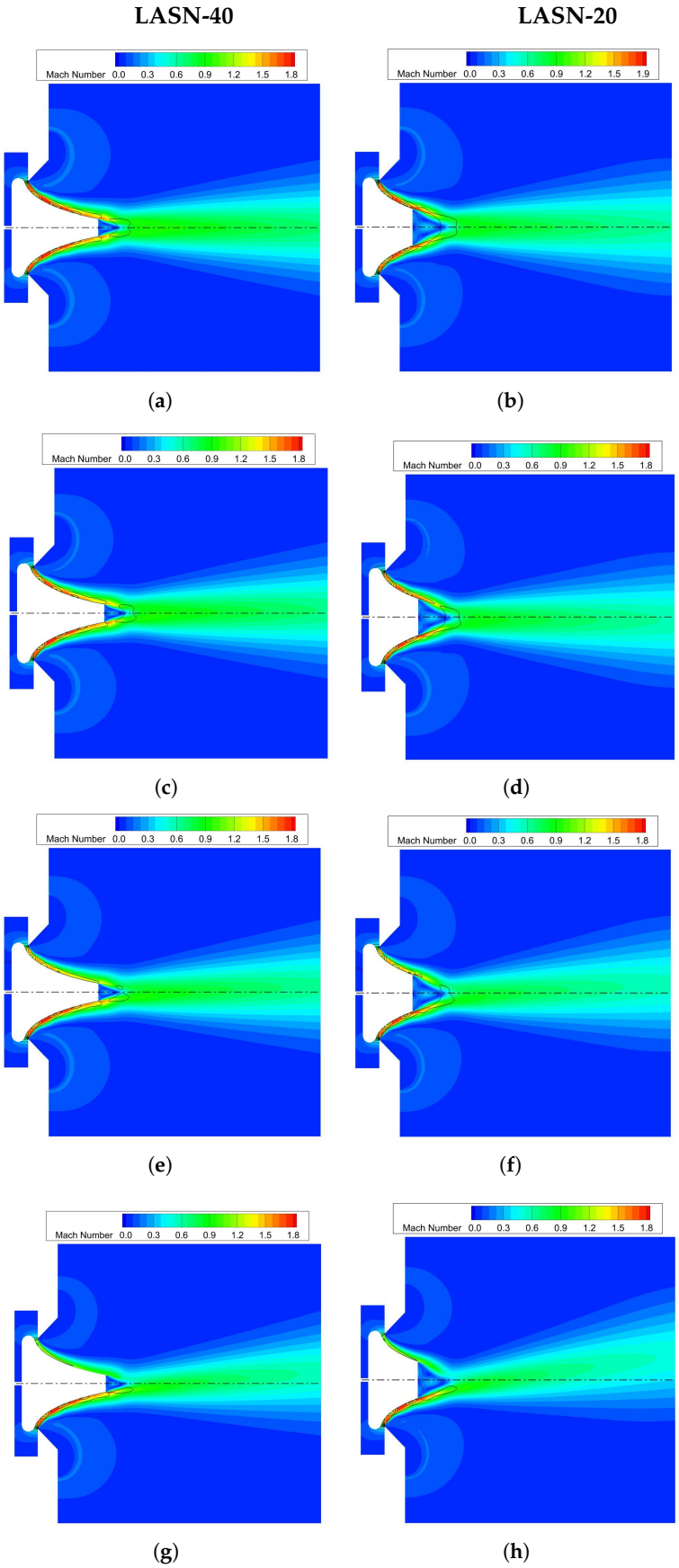

Figure 13. Differential throttling. Mach number contours of the flowfield of LASN-40 (**left**) and LASN-20 (**right**) aerospikes for different DF-values at NPR = 5. (**a**) *DF* = 0. (**b**) *DF* = 0. (**c**) *DF* = 10%. (**d**) DF = 10%. (**e**) *DF* = 25%. (**f**) *DF* = 25%. (**g**) *DF* = 50%. (**h**) *DF* = 50%.

Let us note that when applying differential throttling, in all the tests performed in the present investigation, the bottom outlet is maintained at a fixed value of NPR, i.e., $\mathrm{NPR}_B = 5$ in this case, whereas the upper chamber pressure is decreased according to Equation (1), that is,

$$\mathrm{NPR}_T = (1 - 0.01\,DF)\mathrm{NPR}_B \tag{3}$$

Consequently, as DF increases, the flow approaches the plug upper wedge with a lower and lower speed with respect to that on the bottom surface. As $P_T = \mathrm{NPR}_T P_a$, the primary expansion at the nozzle outlet is also weaker on the upper surface of the plug rather than the bottom, which alters the resultant force on the nozzle and the direction of the thrust. As a combined result, we expect a deflection of the flow and plume upwards.

The bigger the wake, the higher the effect. This can be appreciated in the Figure 13 by comparing the DF effect on the LASN-40 to that on the LASN-20, where the recirculation zone on the plug base is bigger. The effect on the flow deflection is more pronounced on the nozzle with higher truncation (LASN-20).

At higher NPRs, these interactions are amplified because of the stronger reflections that take place on the slip surfaces of the wake.

At $\mathrm{NPR} = 50$, the differences between the wakes produced by the two aerospikes are clearly appreciable, even at $DF = 0$. After that, increasingly complex interactions occurring in the plume regions as the DF increases are appreciable in Figure 14. High values of NPR mean stronger expansions and, therefore, higher flow velocities. Since the plume deflects upwards, the flow encounters a fluid ramp on the top side of the wake, where a flow recompression or shock is formed, and a further expansion on the bottom side of the wake. This effect is amplified as the DF and the pressure mismatch $P_B - P_T$ increase, as shown in Figure 14.

At the design pressure ratio $\mathrm{NPR} = \mathrm{NPR}_d = 200$, the larger recirculation zone on the base of LASN-20 has a strong influence on the plume evolution with respect to the LASN-40 case. The structure of the plume itself is modified by these interactions even in the symmetric, unthrottled case ($DF = 0$). This does not happen in the LASN-40 case, where the recirculations on the plug base are smaller, as shown in Figure 15. In this second case, in fact, the dimensions of the recirculation zone are clearly smaller, with a smaller region of influence that generates perturbations of lower intensity.

By varying the differential throttling parameter DF, the evolution of the flow pattern qualitatively follows the footsteps of that described for $\mathrm{NPR} = 50$, but with interactions of greater intensity that affect larger portions of the flowfield.

4.3.2. Pressure Distributions on the Plug

We now analyze how the parameter DF influences the pressure distribution on the top side and bottom side of the plug at different nozzle pressure ratios. In order to offer a complete scenario, all the results are summarized in Figure 16. The plots are shown separately for the LASN-20 and LASN-40 cases to improve readability.

Only the pressure distributions on the top side are shown. The bottom side pressure is always coincident to that at $DF = 0$. In fact, in the range of NPRs considered, the sub-nozzle throats are always sonic and a supersonic outflow is obtained, which is almost insensitive to what happens on the other side of the plug. However, very close to the truncation wedge, at the plug base, some effects may be produced by the plume deflection.

Another consequence of these considerations is that both LASN-20 and LASN-40 pressure distributions overlap in the region where $X/L_{max} < 0.2$, as already observed for the unthrottled case in Figure 7.

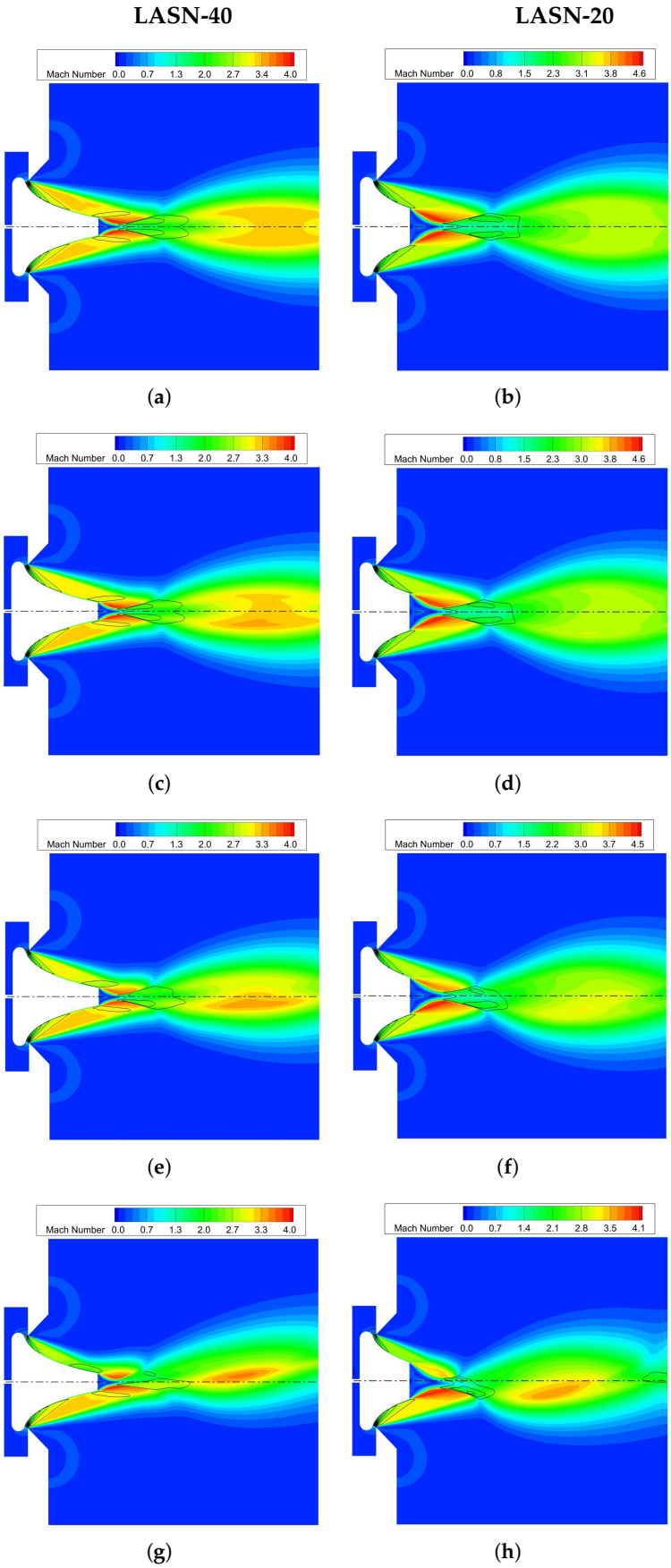

Figure 14. Differential throttling. Mach number contours of the flowfield of LASN-40 (**left**) and LASN-20 (**right**) aerospikes for different *DF*-values at NPR = 50. (**a**) *DF* = 0. (**b**) *DF* = 0. (**c**) *DF* = 10%. (**d**) DF = 10%. (**e**) *DF* = 25%. (**f**) *DF* = 25%. (**g**) *DF* = 50%. (**h**) *DF* = 50%.

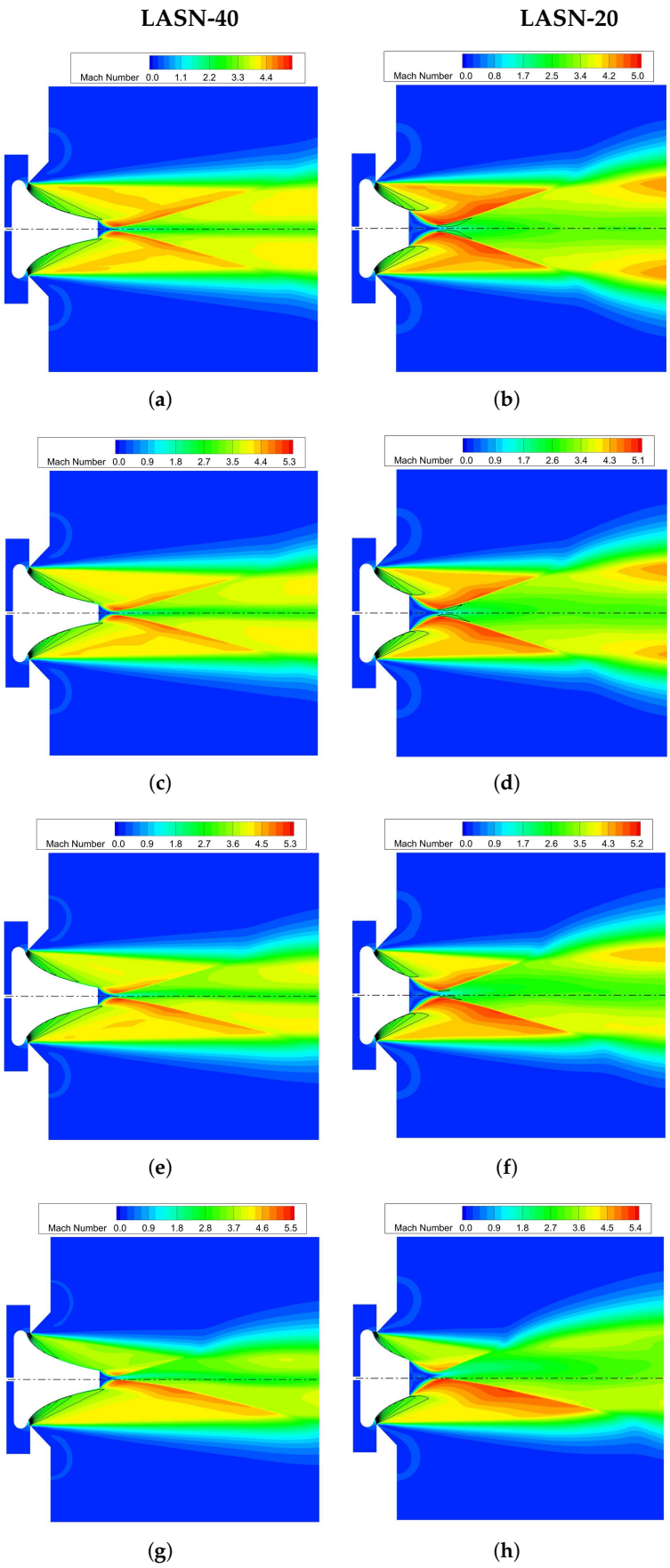

Figure 15. Differential throttling. Mach number contours of the flowfield of LASN-40 (**left**) and LASN-20 (**right**) aerospikes for different DF-values at NPR = 200. (**a**) $DF = 0$. (**b**) $DF = 0$. (**c**) $DF = 10\%$. (**d**) $DF = 10\%$. (**e**) $DF = 25\%$. (**f**) $DF = 25\%$. (**g**) $DF = 50\%$. (**h**) $DF = 50\%$.

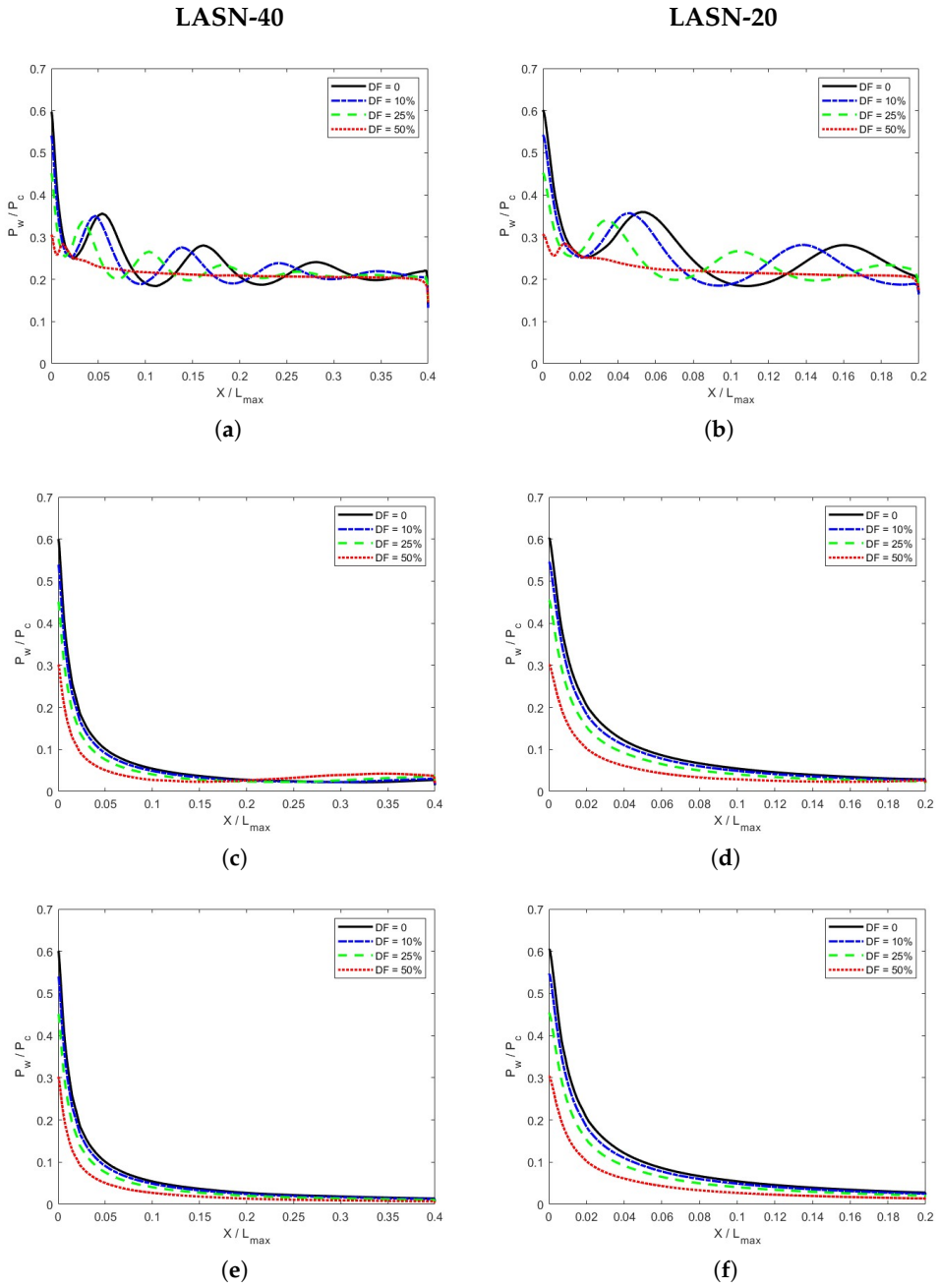

Figure 16. Normalized pressure distribution P_w/P_c over upper and lower surfaces of LASN-40 (**left**) and LASN-20 (**right**) plug at different levels of differential throttling. (**a**) NPR $= 5$. (**b**) NPR $= 5$. (**c**) NPR $= 50$. (**d**) NPR $= 50$. (**e**) NPR $= 200$. (**f**) NPR $= 200$.

At low pressure ratios, e.g., NPR $= 5$, the typical wavy pressure distribution is observed, as in Figure 16a, where the effect of throttling shows an evident shift in pressure maxima toward the left, with a lower and lower peak intensity as far as the DF increases. Although it is not shown here, we also found that the resulting pressure distributions on the top side for $DF = 10\%, 25\%, 50\%$ are very close to the ones characterizing the unthrottled cases with NPR $= 4.5, 3.75, 2.5$, respectively, according to Equation (3). At higher pressure ratios, the primary fan at the cowl lip covers all the plug profile, so that a continuous expansion, without pressure oscillations, is observed.(e.g., see Figure 16c,e). The correspondences between the NPRs of the throttled and unthrottled cases, mentioned above, still holds.

4.3.3. Performances

In view of a control model, differential throttling can be considered a kind of manipulation technique of the nozzle system, where the NPR is a variable defining the interaction of the system with the external ambient, whereas the DF is an internal control variable. The nozzle performances, which are functions of both the nozzle pressure ratio NPR and differential factor DF, are intended as the system output to the control variables. Therefore, the performance computed at each pair (NPR, DF) defines a steady-state working condition, i.e., a "set point". The derivation of a performance map, based on a large number of steady-state conditions computed numerically, is a main goal of the present analysis. The main advantage of the 2D approach is the reduced computational cost needed to generate this performance map.

In this section, we focus on the thrust vectoring results, discussing the effects of differential throttling on the thrust vector components and angle. For clarity, the data are presented separately for each thrust component. The axial component $T_x(\text{NPR}, DF)$ and transversal component $T_y(\text{NPR}, DF)$ are plotted in Figure 17a and Figure 17b, respectively. The results for both aerospikes LASN-20 and LASN-40 are included in these diagrams.

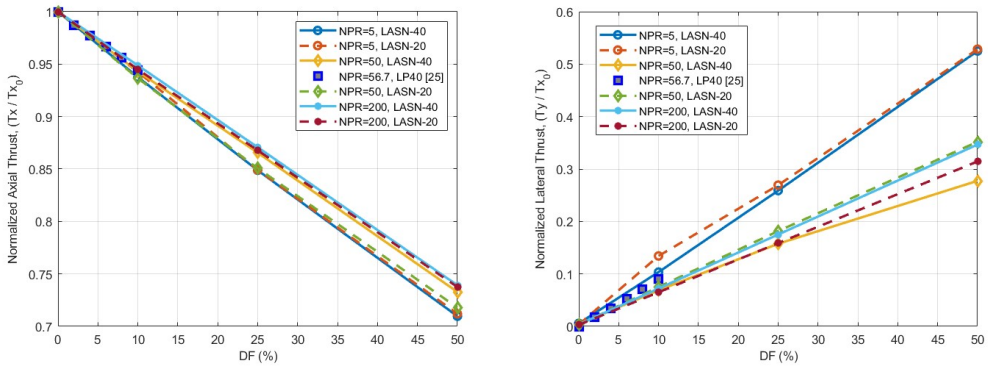

(**a**) (**b**)

Figure 17. Plots of the axial (**a**) and lateral (**b**) thrust components during differential throttling.

For each aerospike, the thrust values are normalized with respect to the thrust in the unthrottled case T_{x0} at the corresponding NPR. This normalization helps to separate the effects of the DF and NPR and, therefore, to distinguish the influence of DF. One may observe, for instance, that all the curves shown in Figure 17 express an almost linear relationship with the DF, while the NPR affects the slope and intercept of each line. A small slope difference is present between the curves concerning the LASN-40 and LASN-20 nozzles. At higher NPRs, the slope differences are less evident.

The axial component of the thrust T_x diminishes almost linearly when DF increases. At the same NPR, the thrust loss is lower for the LASN-40 nozzle with respect to LASN-20, especially at low NPR (see Figure 17a).

The lateral component of the thrust T_y, instead, linearly increases with DF. Looking at Figure 17b, the LASN-20 nozzle is able to generate higher lateral forces than the LASN-40 at the same nozzle pressure ratio.

The ratio of the two thrust components allows us to define a thrust deflection angle $\delta = \tan^{-1}(T_y/T_x)$, used to define the system's ability to direct the thrust. A diagram synthetically reporting the trend in the thrust angle as a function of DF for different NPRs is shown in Figure 18. Again, a proportionality with DF and the thrust angle is observed. The obtainable values are significant (up to $\delta = 36.5^o$) for both aerospikes. The combined effect on the thrust vector angle leads to higher values for the case LASN-20, reported in Figure 18. The thrust deflection still remains linear with DF.

The results of a previous numerical study focused on the FESTIP geometries of the linear aerospike [24], as also reported in Figures 17 and 18. The results computed at NPR = 56.7 are perfectly aligned with those of the LASN-40 and LASN-20 aerospikes of the present study.

As a final consideration, the choice of the most convenient configuration is, however, the result of several considerations and compromises the practical application under consideration. For a rocket, for example, a $\delta \simeq 6^o$ ought to be enough for a typical mission profile [1]. From Figure 18, this thrust angle can be obtained by a DF = 5–20, depending upon the NPR.

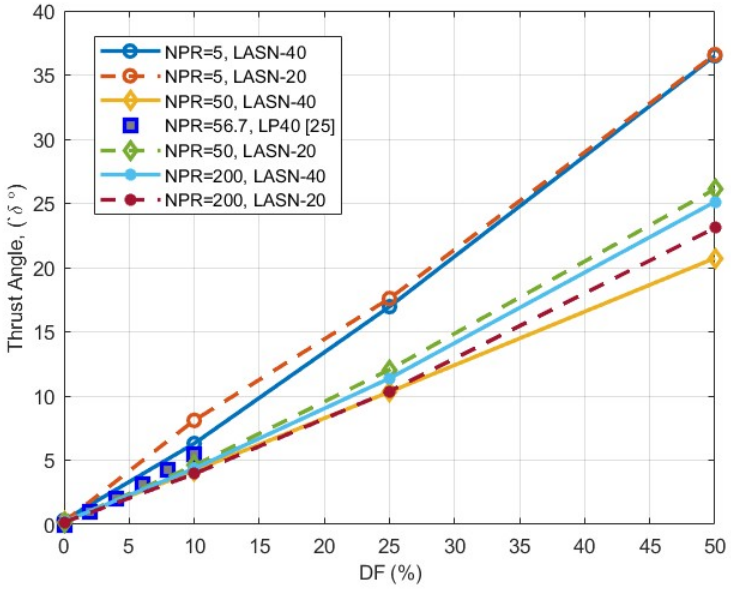

Figure 18. Thrust deflection angle $\delta = \tan^{-1}(T_y/T_x)$ during differential throttling.

5. Conclusions

A comparative analysis on a set of two linear aerospikes nozzles was carried out. The nozzles were generated by truncating the same plug contour at 40% and 20% of its ideal length. The study was based on CFD computations by using a two-dimensional RANS flow model and on the density-based compressible solver, available in Ansys Fluent. The nozzle geometry was extracted from the CAD model of the actual nozzles designed for experimental testing purposes. The work aimed to study the thrust vectoring effectiveness of the designed aerospikes by throttling the nozzle differentially.

The scope of the work was two-fold: (i) to check the ability to capture the complex phenomena occurring on the nozzles within the supposed operative range, up to the design point; (ii) to generate a performance map of the two aerospikes within that range and within the accuracy allowed by a two-dimensional model. A large number of numerical tests were carried out by varying the nozzle pressure ratios and the differential throttling setting. Similarities and differences between the two nozzle flowfields at the same conditions were analyzed and discussed. The comparisons between the numerical and experimental data performed show excellent agreement.

The computed performance maps can be considered a starting point for deriving a dynamic model of the nozzle system. The results obtained provide a solid foundation for the next step, which involves developing a dynamic model for nozzle control. The possibility of using a 2D approach in simulating the unstable response of the system allows us to significantly reduce the computation time and costs of deriving a dynamic model.

Author Contributions: Conceptualization, R.M., G.M.D.C. and M.F.; methodology, J.H., R.M., G.M.D.C. and M.F.; software, J.H.; validation, J.H. and E.R.; formal analysis, J.H.; investigation, J.H., R.M., G.M.D.C., E.R. and M.F.; resources, R.M., G.M.D.C. and M.F.; data curation, J.H. and E.R.; writing—original draft preparation, J.H.; writing—review and editing, J.H., R.M., G.M.D.C. and M.F.; visualization, J.H.; supervision, R.M., G.M.D.C. and M.F. All authors have read and agreed to the published version of the manuscript.

Funding: This research received no external funding.

Data Availability Statement: The datasets presented in this article are not readily available because they are part of an ongoing study; further inquiries can be directed to the corresponding author.

Conflicts of Interest: The authors declare no conflicts of interest.

Abbreviations

NPR	Nozzle Pressure Ratio, NPR $= P_c^o / P_a$
P_c^o	Chamber Total Pressure
P_c	Chamber Static Pressure
P_a	Ambient Pressure
CFD	Computational Fluid Dynamics
RANS	Reynolds-Averaged Navier-Stokes
TVC	Thrust Vectoring Control
FTV	Fluidic Thrust Vectoring
DF	Differential throttling factor, where, $DF = 100 \cdot (1 - \frac{\mathrm{NPR}_T}{\mathrm{NPR}_B})$
LASN-20	Linear AeroSpike Nozzle with plug truncated at 0.2 L_{max}
LASN-40	Linear AeroSpike Nozzle with plug truncated at 0.4 L_{max}
NPR_T	Nozzle Pressure Ratio w.r.t. Top Chamber, P_T^o / P_a
NPR_B	Nozzle Pressure Ratio w.r.t. Bottom Chamber, P_B^o / P_a
P_T^o	Top-Inlet Total Pressure
P_B^o	Bottom-Inlet Total Pressure
P_w	Wall Pressure
L_{max}	Plug ideal length
X_t	Axial coordinate of the start of spike up/down surfaces
T_x	Axial Thrust Component
T_y	Lateral Thrust Component
δ	Thrust Angle, $\delta = \tan^{-1}(T_y / T_x)$

subscripts

B	bottom
T	top
a	ambient
c	chamber
d	design condition
t	sub-nozzle throat/outlet

References

1. Hagemann, G.; Immich, H.; Van Nguyen, T.; Dumnov, G. Advanced rocket nozzles. *J. Propuls. Power* **1998**, *14*, 620–634. [CrossRef]
2. Mason, M.S.; Crowther, W.J. Fluidic thrust vectoring of low observable aircraft. In Proceedings of the CEAS Aerospace Aerodynamic Research Conference, Cambridge, UK, 10–12 June 2002; pp. 1–7. [CrossRef]
3. Deere, K.; Flamm, J.; Berrier, B.; Johnson, S. Computational Study of an Axisymmetric Dual Throat Fluidic Thrust Vectoring Nozzle for a Supersonic Aircraft Application. In Proceedings of the 43rd AIAA/ASME/SAE/ASEE Joint Propulsion Conference & Exhibit, Cincinnati, OH, USA, 8–11 July 2007; AIAA paper 2007-5085. [CrossRef]
4. Warsop, C.; Crowther, W.; Forster, M. NATO AVT-239 Task Group: Supercritical Coanda based Circulation Control and Fluidic Thrust Vectoring. In Proceedings of the AIAA Scitech 2019 Forum, San Diego, CA, USA, 7–11 January 2019; Paper AIAA 2019-0044. [CrossRef]

5. Páscoa, J.; Dumas, A.; Trancossi, M.; Stewart, P.; Vucinic, D. A review of thrust-vectoring in support of a V/STOL non-moving mechanical propulsion system. *Open Eng.* **2013**, *3*, 374–388. [CrossRef]
6. Silver, R. *Advanced Aerodynamic Spike Configurations*; Technical Report; Rocketdyne: Los Angeles, CA, USA, 1966. Available online: https://archive.org/details/DTIC_AD0384855 (accessed on 23 January 2025).
7. Zmijanovic, V.; Leger, L.; Sellam, M.; Chpoun, A. Assessment of transition regimes in a dual-bell nozzle and possibility of active fluidic control. *Aerosp. Sci. Technol.* **2018**, *82–83*, 1–8. [CrossRef]
8. *The Linear Aerospike Engine. From X-33 Prog OFC 8055725801*; NASA: Washington, DC, USA, 1998. Available online: https://archive.org/details/NASA_NTRS_Archive_19990004339 (accessed on 23 January 2025).
9. Haif, S.; Kbab, H.; Bnekhedda, A. Design and Numerical Analysis of a Plug Nozzle. *Adv. Mil. Technol.* **2022**, *17*, 17–32. [CrossRef]
10. Besnard, E.; Chen, H.H.; Mueller, T.; Garvey, J. Design, manufacturing and test of a plug nozzle rocket engine. In Proceedings of the 38th AIAA/ASME/SAE/ASEE Joint Propulsion Conference & Exhibit, Indianapolis, IN, USA, 7–10 July 2002; p. 4038. [CrossRef]
11. Mueller, T.J.; Sule, W.P. Base Flow Characteristics of a Linear Aerospike Nozzle Segment. *J. Eng. Ind.* **1973**, *95*, 353–359. [CrossRef]
12. Takahashi, H.; Munakata, T.; Sato, S. Thrust Augmentation by Airframe-Integrated Linear-Spike Nozzle Concept for High-Speed Aircraft. *Aerospace* **2018**, *5*, 19. [CrossRef]
13. Hao, Z.; Tian, H.; Guo, Z.; Hedong, L.; Li, C. Numerical and experimental investigation of throttleable hybrid rocket motor with aerospike nozzle. *Aerosp. Sci. Technol.* **2020**, *106*, 105983. [CrossRef]
14. D'Agostino, M.; Lee, Y.; Wang, T.; Tuner, J. X-33 XRS-2200 Linear Aerospike Engine Sea Level Plume Radiation. In Proceedings of the 26th JANNAF Exhaust Plume Technology Subcommittee Meeting, San Antonio, TX, USA, 5–9 November 2001.
15. Bach, C.; Schongarth, S.; Bust, B.; Propst, M.; Sieder-Katzmann, J.; Tajmar, M. How to steer an aerospike. In Proceedings of the 69th International Astronautical Congress (IAC), Bremen, Germany, 1–5 October 2018.
16. Ferlauto, M.; Marsilio, R. Open and Closed-Loop Responses of a Dual-Throat Nozzle during Fluidic Thrust Vectoring. In Proceedings of the 52nd AIAA/SAE/ASEE Joint Propulsion Conference, Salt Lake City, UT, USA, 25–27 July 2016; American Institute of Aeronautics and Astronautics: Reston, VA, USA, 2016. [CrossRef]
17. Ferlauto, M.; Marsilio, R. Computational Investigation of Injection Effects on Shock Vector Control Performance. In Proceedings of the 2018 Joint Propulsion Conference, Cincinnati, OH, USA, 9–11 July 2018; American Institute of Aeronautics and Astronautics: Reston, VA, USA, 2018. [CrossRef]
18. Xu, J.; Gu, R.; Huang, S. Exploring the impact of vector thrust on aircraft maneuverability utilizing bypass dual throat nozzle technology. *Aerosp. Sci. Technol.* **2025**, *156*, 109765. [CrossRef]
19. Sazonov, Y.A.; Mokhov, M.A.; Gryaznova, I.V.; Voronova, V.V.; Tumanyan, K.A.; Konyushkov, E.I. Solving Innovative Problems of Thrust Vector Control Based on Euler's Scientific Legacy. *Civ. Eng. J.* **2023**, *9*, 2868–2895. [CrossRef]
20. Saadia, A.; Tariq, A.K. Techniques of Fluidic Thrust Vectoring in Jet Engine Nozzles: A Review. *Energies* **2023**, *16*, 5721. [CrossRef]
21. Das, A.K.; Acharyya, K.; Mankodi, T.K.; Saha, U.K. Fluidic Thrust Vector Control of Aerospace Vehicles: State-of-the-Art Review and Future Prospects. *J. Fluids Eng.* **2023**, *145*, 080801. [CrossRef]
22. Dorau, T.; Propst, M.; Gruber, S.; Selbmann, A.; Joseph, A.G.; Sieder-Katzmann, J.; Buchholz, M.; Sobczak, K.; Soller, S.; Tajmar, M.; et al. Development of an additively manufactured hydrogen peroxide/kerosene 6kN aerospike breadboard engine. In Proceedings of the 72nd International Astronautical Congress (IAC), Dubai, United Arab Emirates, 25–29 October 2021; Volume C4.
23. Eilers, S.; Wilson, M.; Whitmore, S.; Peterson, Z. Side-force amplification on an aerodynamically thrust-vectored aerospike nozzle. *J. Propuls. Power* **2012**, *28*, 811–819. [CrossRef]
24. Ferlauto, M.; Ferrero, A.; Marsicovetere, M.; Marsilio, R. Differential Throttling and Fluidic Thrust Vectoring in a Linear Aerospace. *Int. J. Turbomach. Power* **2021**, *6*, 8. [CrossRef]
25. Hamedi-Estakhrsar, M.; Ferlauto, M.; Mahdavy-Moghaddam, H. Numerical study of secondary mass flow modulation in a Bypass Dual-Throat Nozzle. *Proc. Inst. Mech. Eng. Part G J. Aerosp. Eng.* **2020**, *235*, 488–500. [CrossRef]
26. Resta, E.; Marsilio, R.; Ferlauto, M. Thrust vectoring of a fixed axisymmetric supersonic nozzle using the Shock-Vector Control method. *Fluids* **2021**, *6*, 441. [CrossRef]
27. Marsilo, R.; Di Cicca, G.M.; Resta, E.; Ferlauto, M. Characterization of the Three-Dimensional Flowfield over a Truncated Linear Aerospike. *Fluids* **2024**, *9*, 179. [CrossRef]
28. Resta, E.; Marsilio, R.; Ferlauto, M. Influence of Hot Flow Conditions on Nozzle Performances. In Proceedings of the AIAA SCITECH 2023 Forum, National Harbor, MD, USA & Online, 23–27 January 2023. [CrossRef]
29. Resta, E.; Marsilio, R.; Ferlauto, M. Numerical Investigation of the Burner-Nozzle Interaction on Fluidic Thrust Vectoring. In Proceedings of the AVIATION 2022 Forum, Chicago, IL, USA and Online, 27 June–1 July 2022. [CrossRef]
30. Angelino, G. Approximate method for plug nozzle design. *AIAA J.* **1964**, *2*, 1834–1835. [CrossRef]

31. Di Cicca, G.M.; Hassan, J.; Resta, E.; Marsilio, R.; Ferlauto, M. Experimental Characterization of a Linear Aerospike Nozzle Flow. In Proceedings of the 2023 IEEE 10th International Workshop on Metrology for AeroSpace (MetroAeroSpace), Milan, Italy, 19–21 June 2023; IEEE: New York, NY, USA, 2023. [CrossRef]
32. Di Cicca, G.M.; Marsilio, R.; Resta, E.; Hassan, J.; Ferlauto, M. A Framework for Testing Differential Throttling in Linear Aerospike Nozzle. In Proceedings of the 2024 11th International Workshop on Metrology for AeroSpace (MetroAeroSpace), Lublin, Poland, 3–5 June 2024; IEEE: New York, NY, USA, 2024; pp. 382–387. [CrossRef]
33. *Ansys Fluent Theory Guide. Release 2022 R2*; Ansys Inc.: Canonsburg, PA, USA, 2022.
34. Allmaras, S.; Johnson, F. Modifications and clarifications for the implementation of the Spalart-Allmaras turbulence model. In Proceedings of the Seventh International Conference on Computational Fluid Dynamics (ICCFD7), Big Island, HI, USA, 9–13 July 2012; pp. 1–11.
35. Tian, C.; Lu, Y. Turbulence Models of Separated Flow in Shock Wave Thrust Vector Nozzle. *Eng. Appl. Comput. Fluid Mech.* **2013**, *7*, 182–192. [CrossRef]
36. Poinsot, T.; Lele, S. Boundary conditions for direct simulations of compressible viscous flows. *J. Comput. Phys.* **1992**, *101*, 104–129. [CrossRef]